

## Defected vanadium bronzes as superb cathodes in aqueous zinc-ion batteries

Jianwei Li<sup>1</sup>, Ningjing Luo<sup>2</sup>, Feng Wan<sup>1</sup>, Siyu Zhao<sup>1</sup>, Zhuangnan Li<sup>1</sup>, Wenyao Li<sup>1,3,5</sup>, Jian Guo<sup>1</sup>, Paul R. Shearing<sup>3</sup>, Dan J.L. Brett<sup>3</sup>, Claire J. Carmalt<sup>1</sup>, Guoliang Chai<sup>2\*</sup>, Guanjie He<sup>1,3,4\*</sup> and Ivan P. Parkin<sup>1\*</sup>

<sup>1</sup>Christopher Ingold Laboratory, Department of Chemistry, University College London, 20 Gordon Street, London WC1H 0AJ, U.K. Email: [g.he@ucl.ac.uk](mailto:g.he@ucl.ac.uk); [i.p.parkin@ucl.ac.uk](mailto:i.p.parkin@ucl.ac.uk)

<sup>2</sup>State Key Laboratory of Structural Chemistry, Fujian Institute of Research on the Structure of Matter, Chinese Academy of Sciences (CAS), Fuzhou, 350002 Fujian, P.R. China. Email: [g.chai@fjirsm.ac.cn](mailto:g.chai@fjirsm.ac.cn)

<sup>3</sup>Electrochemical Innovation Lab, Department of Chemical Engineering, University College London, London WC1E 7JE, U.K.

<sup>4</sup>School of Chemistry, University of Lincoln, Joseph Banks Laboratories, Green Lane, Lincoln, LN6 7DL, U.K.

<sup>5</sup>School of Materials Engineering, Shanghai University of Engineering Science, Shanghai 201620, China.

### Abstract

There is a growing need for fast, efficient, safe, low-cost energy storage. Aqueous zinc-ion batteries (AZIBs) may be able to address this need but suffer from fast capacity fade and poor ion diffusion kinetics; due to unstable structures and non-optimised interspacing of layered cathode materials. Herein, we propose a structural engineering strategy by synergistically inducing anionic defects and cationic groups within vanadium bronze structures to improve kinetics and boost capacity. The materials discovered and used as the cathodes in AZIBs presented a high capacity of 435 mAh g<sup>-1</sup> at a current density of 0.2 A g<sup>-1</sup> and excellent stability showing 95% capacity retention after 1500 cycles at 10A g<sup>-1</sup>. This combined experimental and computational study systemically indicated that rapid Zn<sup>2+</sup> storage was achieved from both a highly porous structure, enlarged d-spacing combined with improved electron conductivity as determined by density of states calculations. The modification of vanadium bronze type

cathodes achieved by controlled pre-intercalated species and tailored oxygen deficiency open up an avenue for illumination of superior material design, which is realized and proved its feasibility in this work.

## 1. Introduction

The extensive concerns of limited resources, safety and the environmental issues of current energy storage techniques has fired new research to sustainable battery revolution to satisfy the burgeoning global market.<sup>1</sup> Alkali metal batteries have achieved dramatic progresses in improving safety through introducing all-solid-state<sup>2,3</sup> or water-in-salt electrolyte<sup>4,5</sup> concepts, however the specific capacity still maintain inadequate ( $< 200 \text{ mAh g}^{-1}$ ) and technical issues such as the poor ionic conductivity and high-cost of concentrated metal salts limit their practical applications<sup>6,7,8,9</sup>. Aqueous zinc-ion batteries (AZIBs), a promising candidate for the next-generation of energy storage devices, possess a high theoretical capacity of  $820 \text{ mAh g}^{-1}$  based on zinc anodes and a suitable redox potential of  $-0.76 \text{ V vs. standard hydrogen electrode (SHE)}$ , which have shown a competitive performance when utilizing mild aqueous electrolytes<sup>10,11</sup>. However, the challenge remains of designing suitable cathodes still exist because of the relatively large radii of intercalated hydrated  $\text{Zn}^{2+}$  and a strong electrostatic force between divalent  $\text{Zn}^{2+}$  and host structures<sup>12,13</sup>. To date, various types of cathodes have been developed for AZIBs such as Prussian blue analogs, manganese and vanadium oxide based cathodes<sup>14</sup>. Among them, vanadium-based cathodes exhibit a high theoretical capacity ( $>300 \text{ mAh g}^{-1}$ ) because of the active valence states of V (III to V) during the zinc (de)intercalation process<sup>15</sup>. Additionally, layered crystal structures of cathodes can offer two-dimensional open channels for fast ion diffusion,<sup>16,17,18</sup> which can be modified by the pre-intercalation of foreign cations, forming expanded interlayer spacing materials such as metal dichalcogenide,<sup>19</sup> birnessite manganese oxides<sup>20</sup> and vanadium bronzes<sup>21</sup>, the electrochemical properties were shown to be improved.<sup>22,23,24</sup> different attempts based on vanadium based cathodes having been reported, the developed materials suffer from inadequate reversibility and rate performance due to the strong electrostatic induced collapse and low electron conductivity of vanadium bronzes<sup>25</sup>. Meanwhile, notwithstanding well-proven optimization of battery performance *via* cathode-electrolyte interfacial modification widely observed in lithium ion batteries,<sup>26,27</sup>

similar investigations in AZIBs are still rather limited. In addition, introducing lattice water into vanadium based cathodes for AZIBs have been intensively investigated to significantly reduce the effective charge of  $\text{Zn}^{2+}$  by forming a shield of hydroxyl groups or/and water molecules coordinated with the aqueous media. Thus, a lower activation energy is required for the interfacial transfer and less electrostatic interaction.<sup>28,29,30,31,32</sup> Likewise, there is few reported work on vanadium oxides which suggested tailored electronic structures for facilitating mass transfer properties *via* introducing oxygen deficiencies.<sup>33,34</sup> Therefore, it is necessary to explore a general route for further boosting energy storage properties of vanadium bronze structures by overcoming their inherent deficiencies and unravel its mechanism for unlocking the potential for practical applications.

Herein, we deliberately introduced rich defects, including oxygen deficiency, foreign cation and lattice water, into the fluoride-etched porous vanadium pentoxide framework to form a distinct ammonium vanadium bronze associated with the  $\text{NH}_4\text{V}_4\text{O}_{10}$  (NVO) structure and used this as cathode for AZIBs. The tailored oxygen-deficient hydrated  $\text{NH}_4\text{V}_4\text{O}_{10}(\text{O}_d\text{-NVO}\cdot n\text{H}_2\text{O})$  with large specific surface area gained remarkable improvement in the  $\text{Zn}^{2+}$  diffusion kinetics and enlarged accessible sites for inserted  $\text{Zn}^{2+}$ . This benefits from not only a highly porous microstructure and a further expanded interlayer space for optimized interfacial properties compared with NVO, but also enriched defects within the host framework for tuning electronic structures and lowering ionic diffusion energy barrier. Thus, the corresponding AZIBs illustrate a specific capacity of  $435 \text{ mAh g}^{-1}$  at the current density of  $0.2 \text{ A g}^{-1}$  and 106.5% capacity retention after 1500 cycles under a current density of  $10 \text{ A g}^{-1}$  ( $244 \text{ mAh g}^{-1}$  attained compared to  $229 \text{ mAh g}^{-1}$  at 2<sup>nd</sup> cycle). More impressively, the as-developed  $\text{O}_d\text{-NVO}\cdot n\text{H}_2\text{O}$  improved the rate performance from 19% to 43% of capacity retention as the current density was raised 28 folds compared with the original NVO. A two-pronged mechanism of zinc (de)intercalation facilitated by both oxygen defects and interplanar engineering was carefully clarified by both experimental and computational approaches, which suggest a universal strategy to design high-performance vanadium-based oxides. This also provides deep insight for understanding the synergistic effect of both oxygen vacancies and  $\text{NH}_4^+/\text{H}_2\text{O}$  “pillar” functionalities.

## 2. Result and discussion

The synthesis of both NVO and  $O_d\text{-NVO}\cdot n\text{H}_2\text{O}$  was achieved by a facile hydrothermal reaction (Experimental section). The increased amounts of oxalic acid and  $\text{NH}_4\text{F}$  were employed in the preparation of  $O_d\text{-NVO}\cdot n\text{H}_2\text{O}$ , which generated distinct morphological changes from flower-like architectures to urchin-like nano-ribbons compared with the as-obtained NVO, as shown by scanning electron microscopy (SEM) in Figure 1a,b. Furthermore, in contrast to the observation by transmission electron microscopy (TEM) of NVO (Fig. S1), the characterization depicted a relatively porous microstructure with clear lattice plane indexed to the (205) facet in the  $O_d\text{-NVO}\cdot n\text{H}_2\text{O}$  material as shown in Figure 1c. The porosity is likely the result of enriched defects and etching of the microstructure through the synergy of reducing reagents and  $\text{NH}_4\text{F}$  as precursors.<sup>35,36</sup> For further evaluation of porosity in the as-prepared samples, BET measurement was carried out, which strongly verified a relatively larger specific surface area of  $57.1\text{ m}^2\text{ g}^{-1}$  in  $O_d\text{-NVO}\cdot n\text{H}_2\text{O}$  compared with  $20.6\text{ m}^2\text{ g}^{-1}$  in NVO. In addition, the pore size distribution indicates that the majority of pore diameters were 2 nm which corresponded well with observations from the HRTEM image (Fig. S2). As indicated by X-ray diffraction (XRD) in Figure 1d, the XRD pattern of NVO was indexed to the monoclinic crystalline phase of  $\text{NH}_4\text{V}_4\text{O}_{10}$  (JCPDS: 31-0075) in  $C_2/m$  space group, which was composed of bilayers of V-O polyhedral stacking along the  $c$ -axis and pre-intercalated  $\text{NH}_4^+$  accommodated within the interplanar sites.<sup>37</sup> Similarly, the  $O_d\text{-NVO}\cdot n\text{H}_2\text{O}$  possesses the corresponding features of diffraction peaks but with a slight shift to lower  $2\theta$  values, as observed in the (001) facet ( $2\theta=3.905^\circ$ ), which suggests an expanded interlayer spacing along the  $c$ -axis of  $10.4\text{ \AA}$  compared with as-prepared NVO ( $9.6\text{ \AA}$ ), according to Bragg's equation. Moreover, commercial  $\text{V}_2\text{O}_5$  (JCPDS: 41-1426) was also adopted as a comparable material to explore the effects of pre-intercalated  $\text{NH}_4^+$  in  $\text{V}_2\text{O}_5$  frameworks on AZIBs performance. Figure 1e exhibits the Fourier transform infrared spectrum (FTIR) of NVO,  $O_d\text{-NVO}\cdot n\text{H}_2\text{O}$  and commercial  $\text{V}_2\text{O}_5$ , respectively. It can be clearly seen that the absorption bands of the materials have a series of similar vibrational modes which can be assigned to V-O bending, V-O-V stretching and V=O stretching at the wave-numbers of  $472\text{ cm}^{-1}$  ( $454\text{ cm}^{-1}$ ),  $756\text{ cm}^{-1}$  ( $744\text{ cm}^{-1}$ ) and  $987\text{ cm}^{-1}$  ( $945\text{ cm}^{-1}$ ) for  $O_d\text{-NVO}\cdot n\text{H}_2\text{O}$  (and NVO), respectively.<sup>38,39</sup> The slight red shift of characteristic FTIR bands at V=O stretching mode in as-prepared samples compared with commercial  $\text{V}_2\text{O}_5$  could be attributed to the pre-intercalated species bonded with apical oxygen in  $\text{VO}_x$

polymorphs. The result corresponds to the observation of linear expansion of (001) d-spacing in the XRD results, and agrees with previous reported work on  $\text{Li}^+$  pre-intercalated  $\text{V}_2\text{O}_5$ .<sup>40</sup> In particular, the bands around 1412 and 3177  $\text{cm}^{-1}$  conform to the symmetric bending and asymmetric stretching modes of N-H, respectively,<sup>37</sup> which confirm that the  $\text{NH}_4^+$  exists in both NVO and  $\text{O}_d\text{-NVO}\cdot\text{nH}_2\text{O}$  materials. Moreover, it is seen that there are two distinct bands at 1644 and 3556  $\text{cm}^{-1}$  corresponding to the bending and stretching modes of H-O, respectively,<sup>41</sup> which indicate the presence of  $\text{H}_2\text{O}$  in  $\text{O}_d\text{-NVO}\cdot\text{nH}_2\text{O}$ . Thermal gravimetric analyzer (TGA) was carried out to evaluate the mass loss during the elevation of temperature. It needs to be emphasized that the partial  $\text{NH}_4^+$  species could also escape from the framework accompany with the water. Therefore, it is difficult to extract the actual amount of water content from the TGA measurement. However, the plot in Fig. S3 indicates a greater weight loss in the sample of  $\text{O}_d\text{-NVO}\cdot\text{nH}_2\text{O}$  compared with NVO. Further confirmation of the  $\text{NH}_4^+$  is provided from the presence of N *via* X-ray photoelectron spectroscopy (XPS), which is depicted in Figure 1f and shows a clear N 1s core level spectrum for both NVO and  $\text{O}_d\text{-NVO}\cdot\text{nH}_2\text{O}$  materials. For quantitative analysis of N elemental concentration in the as-prepared materials, relative sensitivity factors were used to calculate the varied amount of  $\text{NH}_4^+$  species, interpreted as a ratio of N:V, which showed 1:3.94 for NVO and 1:3.9 for  $\text{O}_d\text{-NVO}\cdot\text{nH}_2\text{O}$ , suggesting a negligible change in N concentration through the specific modification. In addition, the V 2p core-level spectrum next to N 1s spectrum shows mixed oxidation states of V compared with that in commercial  $\text{V}_2\text{O}_5$  (Figure 1g), which indicate that a partial reduction of  $\text{V}^{5+}$  species has occurred when introducing extraneous cations into the  $\text{V}_2\text{O}_5$  frameworks. More specifically, the peaks with binding energy of  $517.3 \pm 0.2$  eV in all three materials refer to  $\text{V}^{5+} 2p_{3/2}$ , while a lower binding energy of 516.1 eV was assigned to  $\text{V}^{4+} 2p_{3/2}$  and only observed in NVO and  $\text{O}_d\text{-NVO}\cdot\text{nH}_2\text{O}$ . The same results of mixed valence states can be also found in other reported works on pre-intercalated vanadium oxides.<sup>42,43,44</sup> Furthermore, proportion calculations of varied V species peak areas indicate that the average oxidation states were  $\text{V}^{4.65+}$  and  $\text{V}^{4.74+}$  for  $\text{O}_d\text{-NVO}\cdot\text{nH}_2\text{O}$  and NVO, respectively. The relatively lower valence state of V species in  $\text{O}_d\text{-NVO}\cdot\text{nH}_2\text{O}$  was anticipated since more reducing reagent was applied in the preparation process resulting in oxygen deficiency induced reduction of V oxidation states, which is discussed in the DFT analysis (*vide infra*). Figure 1h illustrates the O 1s core

level spectrum of all materials. It is noteworthy that significant defective oxygen species peaks in both  $O_d\text{-NVO}\cdot n\text{H}_2\text{O}$  and NVO with a binding energy of 531.6 eV, which is in good agreement with previous reports of oxygen defects in vanadium oxide based materials.<sup>45,46,47,48</sup> Moreover, the proportion of defective oxygen concentration in  $O_d\text{-NVO}\cdot n\text{H}_2\text{O}$  was much higher than that in NVO which can be simplified by comparison of the ratio between two oxygen species peaks area within the O 1s spectrum ( $O_d: O_v$  is 27:73 for NVO and 43:57 for  $O_d\text{-NVO}$ , respectively). Further evidence of existed oxygen deficiency was verified by electron paramagnetic resonance (EPR; Fig. S4a), which illustrated a signal at  $g \approx 1.98$  assigned to the unsaturated oxygen species (oxygen vacancies) in the spectrum. It should be noted that there was no trace of  $F^-$  species observed from both XPS survey and core level of F 1s spectra in  $O_d\text{-NVO}\cdot n\text{H}_2\text{O}$  (Fig. S4b,c). However, the addition of  $\text{NH}_4\text{F}$  is crucial not only to produce a highly porous microstructure, but also for adjusting appropriate pH value and concentration of vanadyl species in aqueous solution during the preparation process (Fig. S5). As a consequence, it can be seen that some impurity phases can be evidently distinguished from the XRD of a control sample of  $O_d\text{-NVO}\cdot n\text{H}_2\text{O}$  without the additional  $\text{NH}_4\text{F}$  in preparation process (Fig. S6). At this stage note that the partial occupancy of N sites results in many potential geometry structures of NVO. Subsequently, the  $1 \times 3 \times 1$  supercell of NVO was built to eliminate interactions between images for DFT calculations. We have calculated the total energies of the different configurations of  $\text{NH}_4\text{V}_4\text{O}_{10}$  and the structure with the lowest total energy is illustrated in Figure 1i. Three  $\text{NH}_4^+$  forms the N-H...O hydrogen bonds with adjacent O atom. Among them, two  $\text{NH}_4^+$  are close to each other while the third one is far away from them. All three  $\text{NH}_4^+$  locate on different sites but they are close to each other along the (010) orientation (more discussion in the DFT section).

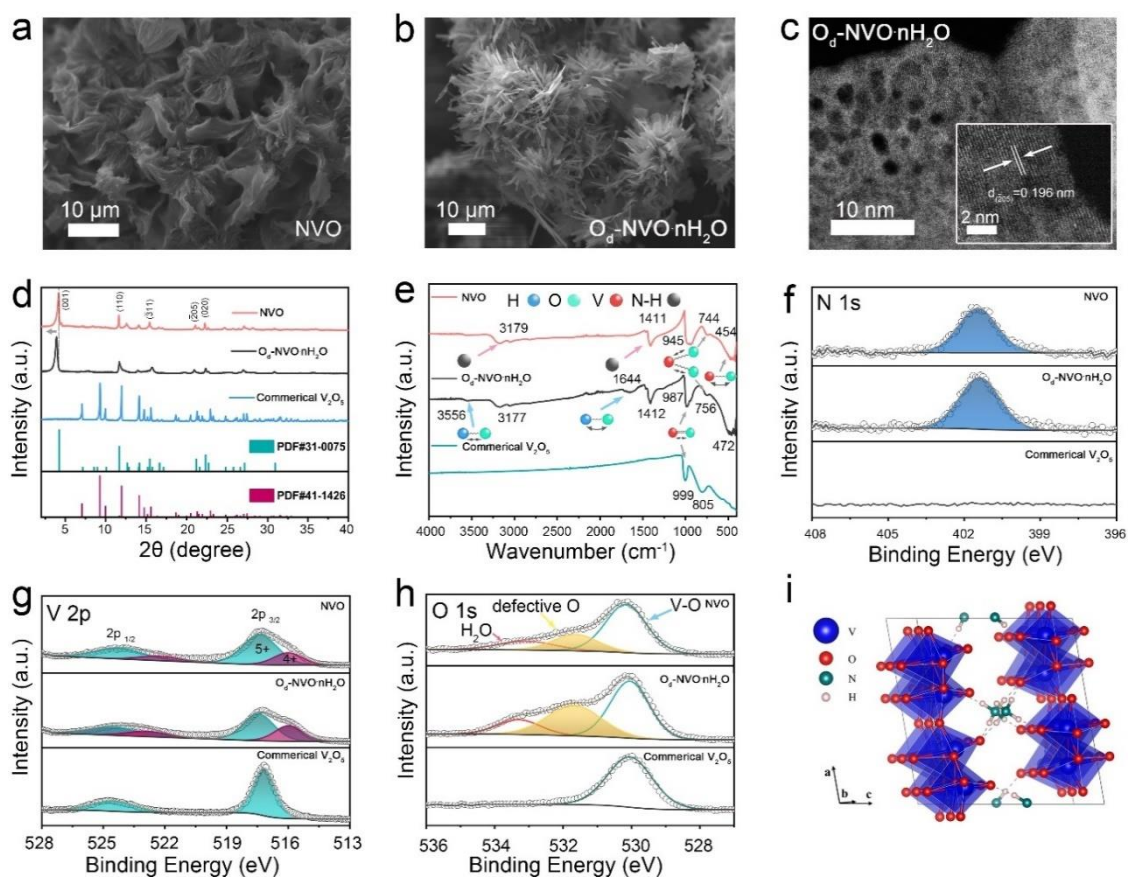


**Figure 1.** SEM images of a) NVO and b)  $O_d$ -NVO· $nH_2O$ ; c) HRTEM of as-obtained  $O_d$ -NVO· $nH_2O$ ; d) XRD patterns and e) FTIR spectra of NVO,  $O_d$ -NVO· $nH_2O$  and commercial  $V_2O_5$ ; XPS spectra of the f) N 1s region, g) V 2p region and h) O 1s region in NVO,  $O_d$ -NVO· $nH_2O$  and commercial  $V_2O_5$ , respectively; i) The most stable geometry of  $NH_4V_4O_{10}$  supercell calculated by GGA+U functional.

The as-obtained NVO,  $O_d$ -NVO· $nH_2O$  and commercial  $V_2O_5$  were assembled for the battery performance evaluation in coin cell configurations. Figure 2a presents galvanostatic charge/discharge (GCD) profiles of NVO and  $O_d$ -NVO· $nH_2O$  under varied applied current densities from 0.5 to 14  $A g^{-1}$ . It is clear that the distinct plateaus in the charge/discharge process can be distinguished in accordance with multiple redox couples of cyclic voltammetry (CV) curves for different anionic/cathodic reactions (Figure 2b). Additionally, a distinct electrochemical reaction behavior can be discerned through comparing the GCD profiles and steady changes of CV profiles in the first three cycles of the batteries, which indicate a relatively larger specific capacity and higher reversibility of  $Zn^{2+}$  intercalation/extraction achieved in  $O_d$ -NVO· $nH_2O$  compared to NVO. In contrast, the CV profile of commercial  $V_2O_5$

shows a dominant anodic peak around 1.3 V, indicating a different electrochemical process during Zn<sup>2+</sup> insertion/extraction (Fig. S7). A further investigation of long cycle measurements under a low current density of 0.2 mA g<sup>-1</sup> also exhibited a better performance of O<sub>d</sub>-NVO·nH<sub>2</sub>O with a maximum specific capacity of 435 mAh g<sup>-1</sup> compared with 405 mAh g<sup>-1</sup> of NVO. Moreover, the cycling stability of O<sub>d</sub>-NVO·nH<sub>2</sub>O shows a 92 % capacity retention after 50 cycles charge/discharge process with a corresponding Coulombic efficiency (CE) over 99%. In contrast, there was 14% decay of capacity in NVO under identical conditions. Comparatively, the battery using commercial V<sub>2</sub>O<sub>5</sub> as the cathode material underwent a long activation process with a gradual increase of specific capacity from an initial capacity of 109 mAh g<sup>-1</sup> to 256 mAh g<sup>-1</sup> after 25 cycles (Fig. S7a). This can be explained *via* sluggish zinc intercalation kinetics in commercial V<sub>2</sub>O<sub>5</sub> electrode existing due to the inadequate interlayer space and shortage of “lubricants” (lattice water/NH<sub>4</sub><sup>+</sup>).<sup>23,49</sup> The rate performance was evaluated by stepwise increase in current densities from 0.5 to 14 A g<sup>-1</sup> and returning to 0.5 A g<sup>-1</sup> with 10 cycles at each current density, respectively. Impressively, the O<sub>d</sub>-NVO·nH<sub>2</sub>O exhibited superior rate capability in Figure 2d and reversibility with a capacity of 406 mAh g<sup>-1</sup> at 0.5 A g<sup>-1</sup> in the initial first 10 cycles and 175 mAh g<sup>-1</sup> at 14 A g<sup>-1</sup>, which can be calculated as 43% capacity retained after 28 fold increase of current densities. Additionally, upon returning to 0.5 A g<sup>-1</sup>, the capacity remains 401 mAh g<sup>-1</sup>, suggesting a much more robust reversibility compared with many reported vanadium-based cathodes which showed significant decay after rate cycling tests.<sup>50,51,52,53,54</sup> In contrast, NVO illustrates inferior rate performance with a capacity of 382 mAh g<sup>-1</sup> at 0.5 A g<sup>-1</sup> and 71 mAh g<sup>-1</sup> at 14 A g<sup>-1</sup>. Thus, there is only 19% capacity retention, revealing a relatively larger energy barrier, thus inhibiting fast Zn<sup>2+</sup> diffusion. Similarly, an unfavorable rate performance of commercial V<sub>2</sub>O<sub>5</sub> can be observed in Fig. S7b, in which, the cell suffers from both low capacity and long activation process. In addition, after 1500 cycling measurements for both NVO and O<sub>d</sub>-NVO·nH<sub>2</sub>O cells under a current density of 10 A g<sup>-1</sup>, the high reversibility with outstanding capacity retention as presented in Figure 2e was verified. Both NVO and O<sub>d</sub>-NVO·nH<sub>2</sub>O showed negligible capacity fading with a clear determination of a specific capacity of 244 mAh g<sup>-1</sup> at the 1500<sup>th</sup> cycle compared with 229 mAh g<sup>-1</sup> at the 2<sup>nd</sup> cycle for O<sub>d</sub>-NVO·nH<sub>2</sub>O cells. Comparatively, 138 mA h g<sup>-1</sup> and 100 mAh g<sup>-1</sup> was observed for the 1500<sup>th</sup> cycle and 2<sup>nd</sup> cycle, respectively, for NVO cells. Moreover, a much longer period of activation

cycling behavior and low capacity performance were observed for the commercial  $V_2O_5$  cell under  $5A\ g^{-1}$  for 1500 cycles (Fig. S7c). The above results imply that the  $O_d\text{-NVO}\cdot nH_2O$  electrode possesses improved reversibility and superior specific capacity, which was implemented with high current densities during charge/discharge process. This can be interpreted as facilitated  $Zn^{2+}$  diffusion kinetics derived from the tailored porous structure and lattice defects. Meanwhile, the introduction of lattice water and  $NH_4^+$  not only offers a charge shielding screen to smooth electrostatic interaction between  $V_2O_5$  sheets and guest  $Zn^{2+}$ , but also contributes to enlarging the bilayer and inhibition of “lattice breathing”.<sup>23,55</sup> The Ragone plot (Fig. S8) illustrates a high energy density of  $288\ Wh\ kg^{-1}$  and an outstanding power density of  $358\ W\ kg^{-1}$  for the  $O_d\text{-NVO}\cdot nH_2O$  electrode, which is superior to previously reported cathodes such as  $Ca_{0.25}V_2O_5\cdot nH_2O$  ( $267\ Wh\ kg^{-1}$ )<sup>56</sup>,  $Zn_{0.25}V_2O_5\cdot nH_2O$  ( $250\ Wh\ kg^{-1}$ )<sup>43</sup>,  $Zn_2V_2O_7$  ( $166\ Wh\ kg^{-1}$ )<sup>57</sup>,  $Zn_3V_2O_7(OH)_2\cdot 2H_2O$  ( $214\ Wh\ kg^{-1}$ )<sup>58</sup>,  $Na_3V_2(PO_4)_2F_3@C$  ( $97.5\ Wh\ kg^{-1}$ )<sup>59</sup> and  $K_2V_8O_{21}$  ( $222.3\ Wh\ kg^{-1}$ )<sup>60</sup>.

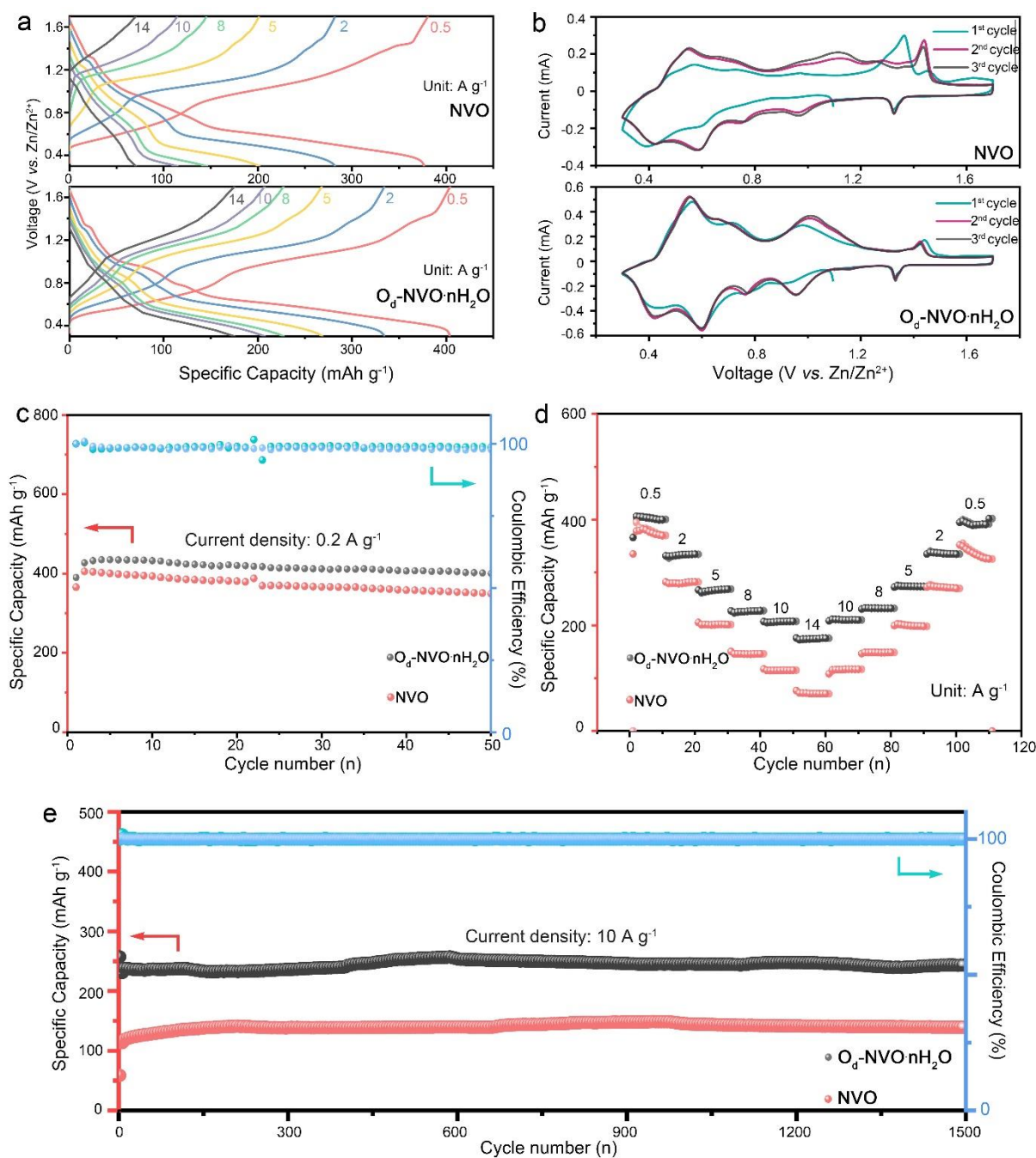


**Figure 2.** a) Galvanostatic charge/discharge profiles for NVO and  $O_d$ -NVO· $nH_2O$  cathodes at different current densities; b) Cyclic voltammetry plots of NVO and  $O_d$ -NVO· $nH_2O$  at a scan rate of  $0.2 mV s^{-1}$  for the first three cycles; c) Long-cycle charge/discharge measurements of NVO and  $O_d$ -NVO· $nH_2O$  cells under the current density of  $0.2 A g^{-1}$ ; d) Rate performance evaluations of NVO and  $O_d$ -NVO· $nH_2O$  cells; e) Long-cycle stability of NVO and  $O_d$ -NVO· $nH_2O$  cells under the current density of  $10 A g^{-1}$ .

To investigate the inherent cycle-dependent ion transport property within the as-developed

electrodes, electrochemical impedance spectroscopy (EIS) was carried out to determine the purely Ohmic resistance ( $R_s$ ) and charge transfer resistance ( $R_{ct}$ ) for both initial and after cycling states. Though analysis of EIS plots in Fig. S9, the summarized results revealed that both NVO and  $O_d$ -NVO· $nH_2O$  possessed relatively lower  $R_s$  (0.64  $\Omega$  and 0.68  $\Omega$  for NVO and  $O_d$ -NVO· $nH_2O$ , respectively, Table S1) compared with commercial  $V_2O_5$  ( $R_s = 1.93 \Omega$ ). Meanwhile, the  $R_{ct}$  of  $O_d$ -NVO· $nH_2O$  ( $R_{ct} = 33.4 \Omega$ ) at the initial state demonstrated a much improved charge transport behavior between electrode and electrolyte compared with assembled NVO ( $R_{ct} = 128.8 \Omega$ ) and  $V_2O_5$  cells ( $R_{ct} = 186.2 \Omega$ ) measured under identical condition, which verifies a dramatically enhanced interfacial engineering of the  $O_d$ -NVO· $nH_2O$  materials. Moreover, the  $R_{ct}$  of  $O_d$ -NVO· $nH_2O$  (22.5  $\Omega$ ) was still much smaller than both NVO and commercial  $V_2O_5$  (NVO:  $R_{ct} = 52.6 \Omega$ , commercial  $V_2O_5$ :  $R_{ct} = 128.8 \Omega$ ) after cycling, which confirms the excellent ionic diffusion kinetics and electrochemical properties benefitting from different types of defects and pre-intercalated guest species. Additionally, evaluation of capacity contributions derived from capacitive and diffusion behavior was investigated for NVO and  $O_d$ -NVO· $nH_2O$  materials, respectively, as shown in Fig. S10. The quantified CV profile (Fig. S10a,b) clearly indicated that there is 74% capacitive contribution among all the current responses at a scan rate of 0.5  $mV s^{-1}$  in  $O_d$ -NVO· $nH_2O$ , which is much higher than that of NVO (43%) under the same sweep rate (Fig. S10c,d). Similarly, a growing fraction of capacitive contribution can be observed as the sweep rates is raised from 0.1 to 1  $mV s^{-1}$  in both electrodes. Therefore, the predominantly capacitive controlled behaviors of  $O_d$ -NVO· $nH_2O$  are responsible for its high-rate capability. Further analysis of CV profiles was carried out by using the following equation:<sup>61</sup>

$$i = a v^b$$

The equation above can be rewritten as  $\log(i) = b \log(v) + \log(a)$ , which is used to describe the relationship between measured peak current ( $i$ ) and the sweep rate ( $v$ ) from CV plots. In particular, the coefficient  $b$  reflects capacitive response if the value =1, whereas an absolute diffusion-controlled kinetic is verified by  $b$ -value equal to 0.5, corresponding to a Faradaic (de)intercalation.<sup>62</sup> Therefore, for both materials, three pairs of redox peaks were calculated, as shown in Fig. S11, and  $b$  values of 0.71, 1.01, 1.04, 0.88, 0.76 and 0.75 were found in  $O_d$ -NVO· $nH_2O$  implying a prevailed surface-controlled capacitive behavior rather than relatively

lower  $b$  value corresponding to mainly diffusion-controlled redox reactions in NVO electrodes ( $b = 0.33, 0.98, 0.92, 0.62, 0.77$  and  $0.71$ , respectively). Moreover, the overpotential gaps of  $O_d\text{-NVO}\cdot n\text{H}_2\text{O}$  between A1(2) and C1(2) redox pairs at each scan rates were smaller than those in NVO, which was attributed to a relatively weaker polarization along with a boosted  $\text{Zn}^{2+}$  insertion/extraction process in  $O_d\text{-NVO}\cdot n\text{H}_2\text{O}$ . In addition to CV analysis of the as-fabricated batteries, the galvanostatic intermittent titration technique (GITT) measurement was utilized to acquire  $\text{Zn}^{2+}$  diffusion coefficients to strengthen the proof of improved kinetics from the multiscale optimizations in  $O_d\text{-NVO}\cdot n\text{H}_2\text{O}$ . The calculated  $D_{\text{Zn}^{2+}}$  during charge/discharge process at each state of zinc extraction/insertion states are illustrated in Fig. S12, which clearly indicate that the  $D_{\text{Zn}^{2+}}$  of  $O_d\text{-NVO}\cdot n\text{H}_2\text{O}$  ( $10^{-8}\text{-}10^{-9}\text{ cm}^2\text{s}^{-1}$ ) is higher than that observed in NVO ( $10^{-9}\text{-}10^{-10}\text{ cm}^2\text{s}^{-1}$ ). Thus, by determining the kinetic behaviors from the CV analysis, the large proportion of pseudocapacitive behaviors of  $O_d\text{-NVO}\cdot n\text{H}_2\text{O}$  effectively demonstrates the feasibility of a promising strategy for improving rate performance and reversibility of cathodes in AZIBs.

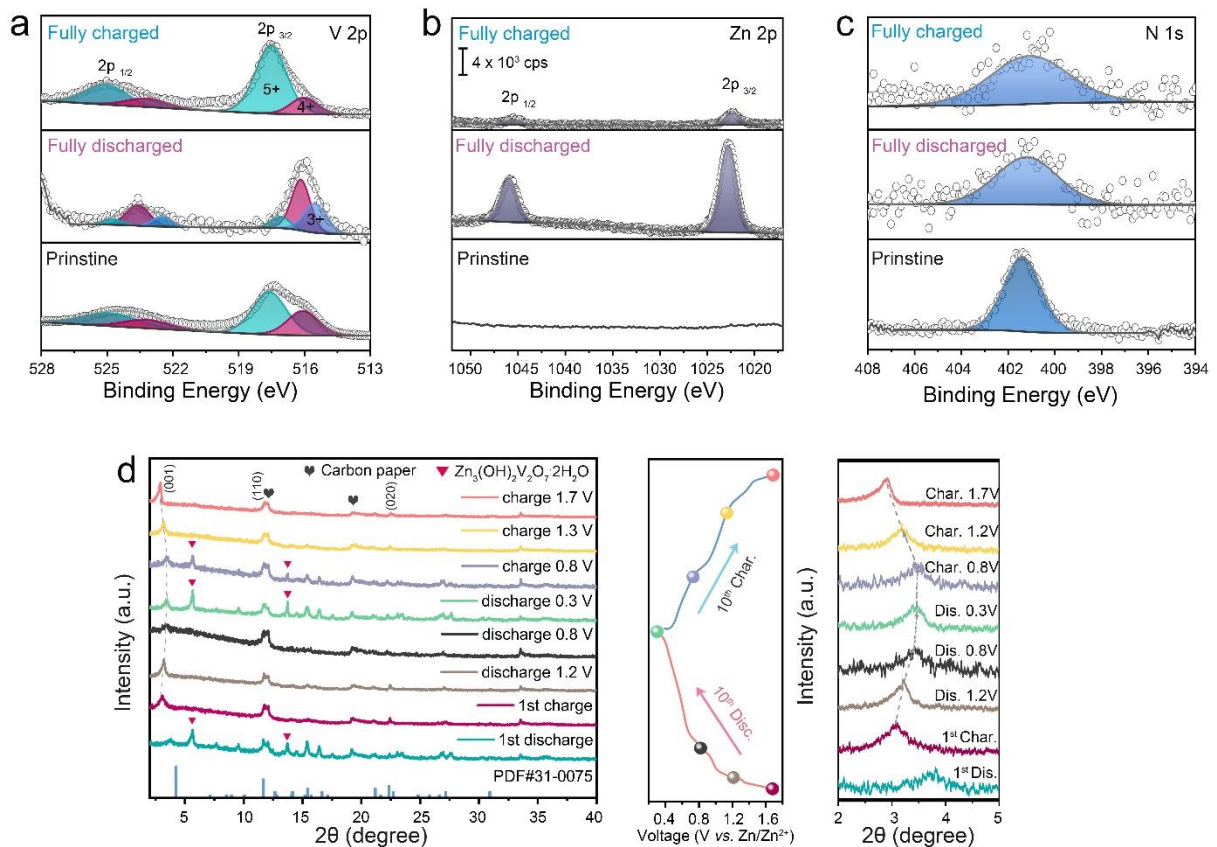


**Figure 3.** *Ex-situ* XPS spectra of a) V 2p, b) Zn 2p and c) N 1s at initial, charge/discharge states of the O<sub>d</sub>-NVO·nH<sub>2</sub>O electrode, respectively; d) XRD patterns of the O<sub>d</sub>-NVO·nH<sub>2</sub>O electrode measured under different charge/discharge states in both 1<sup>st</sup> and 10<sup>th</sup> cycles.

The highly reversible zinc (de)intercalation process in terms of crystal structures and chemical states of O<sub>d</sub>-NVO·nH<sub>2</sub>O materials were evaluated at varied charge/discharge states *via ex-situ* XPS and XRD. Figure 3a shows an obvious reduction of valence states in fully discharged O<sub>d</sub>-NVO·nH<sub>2</sub>O electrodes through an observation of newly emerging V<sup>3+</sup> (2p<sub>3/2</sub>: 515.5 eV) and intensified V<sup>4+</sup> (2p<sub>3/2</sub>: 516.2 eV) components. However, the hybrid V species recovered to their original states, and were slightly more oxidative for fully charged O<sub>d</sub>-NVO·nH<sub>2</sub>O electrodes. The related phenomena are in good accordance with previously reported vanadium based cathode materials.<sup>42,43</sup> In addition, the core level spectrum of Zn 2p in Figure 3b clearly shows that no zinc signal was observed in the pristine cathode. While, a substantive peak (2p<sub>3/2</sub>: 1022.8 eV) in the Zn 2p spectrum was found in the fully discharged electrode, indicating the intercalation of Zn<sup>2+</sup> into the cathodes. After the charge process, the majority of Zn 2p species were deintercalated from the O<sub>d</sub>-NVO·nH<sub>2</sub>O, which presents a pair of subtle peaks related to the Zn 2p sites, consistent with previous studies.<sup>63</sup> Figure 3c confirms that the NH<sub>4</sub><sup>+</sup> species always exist in the cathodes at the same peak position (1s: 401.5 eV) regardless of different states of charge/discharge, which illustrates stable structural support within the bilayers of the VO<sub>x</sub> polyhedral network. As a result, the reversible chemical states and anchored NH<sub>4</sub><sup>+</sup> “pillar” of O<sub>d</sub>-NVO·nH<sub>2</sub>O materials at different conditions validated by *ex-situ* XPS suggests robust electrochemical properties during the Zn<sup>2+</sup> insertion/extraction process.

After clarifying various chemical states during insertion/extraction of Zn<sup>2+</sup> processes, *ex-situ* XRD was employed to investigate the crystal phase evolution of O<sub>d</sub>-NVO·nH<sub>2</sub>O under different charge/discharge states. Figure 3d displays the *ex-situ* characterized XRD pattern of O<sub>d</sub>-NVO·nH<sub>2</sub>O cathode at both the 1<sup>st</sup> and 10<sup>th</sup> cycle at 0.5 A g<sup>-1</sup> with various charge/discharge states according to the plateaus in the GCD curves. It is noteworthy that there is a second reversible phase of Zn<sub>3</sub>V<sub>2</sub>O<sub>7</sub>(OH)<sub>2</sub>·2H<sub>2</sub>O (JCPDS no. 87-0417, space group: P $\bar{3}$ m1) only appearing in the 1<sup>st</sup> and 10<sup>th</sup> discharged states, and likewise observed as weakening diffraction peaks in subsequently multi-cycled electrodes charged at 0.8 V, which has been also widely

identified in previous studies of  $\text{K}_2\text{V}_8\text{O}_{21}$ <sup>60</sup>,  $\text{V}_6\text{O}_{13}\cdot n\text{H}_2\text{O}$ <sup>30</sup> and  $\text{Cu}_{0.1}\text{V}_2\text{O}_5\cdot 0.08\text{H}_2\text{O}$ <sup>42</sup>. Additionally, it is seen that, the (001) reflection sites (shown in a magnified  $2\theta$  region from  $2^\circ$  to  $5^\circ$ ) showed an evidently steady shift to higher  $2\theta$  value referring to a contraction of d-spacing from 13.1 to 10.7 Å from initial charged state to fully discharged state at the 10<sup>th</sup> cycle. Inversely, the interlayer space expands back to lower  $2\theta$  and hence suggests a reduced electrostatic interaction within the bilayers because of the extraction of  $\text{Zn}^{2+}$ .<sup>43</sup> Hence, the reversible phase changes in  $\text{O}_d\text{-NVO}\cdot n\text{H}_2\text{O}$  cathode further validates a robust cycling performance and brings an insight into the zinc storage mechanism from the perspective of its phase evolutions.

To understand the structural difference between  $\text{O}_d\text{-NVO}\cdot n\text{H}_2\text{O}$  and NVO, DFT simulations were adopted to elucidate the formation and relevant properties of oxygen point vacancies in NVO, and the electrostatic interactions of  $\text{Zn}^{2+}$  with oxygen ions. For  $\text{NH}_4\text{V}_4\text{O}_{10}$ , one oxygen was removed from  $1\times 3\times 1$  supercell ( $(\text{NH}_4)_3\text{V}_{24}\text{O}_{60}$ ) to model oxygen point vacancy.

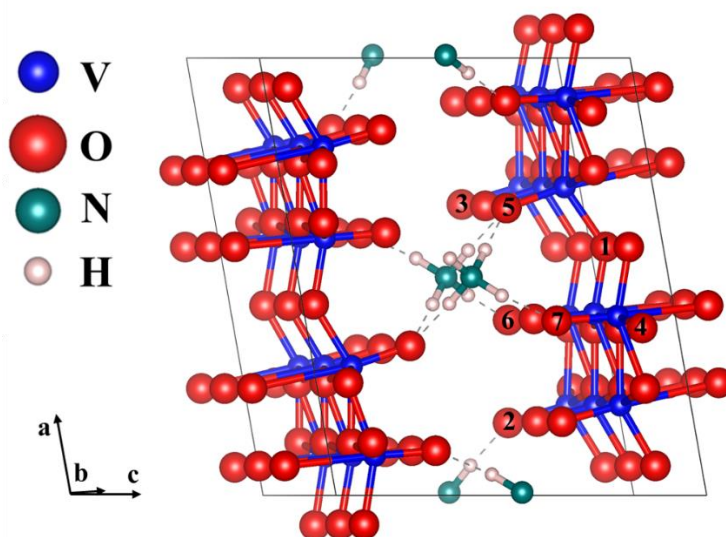


**Figure 4.** The most stable geometry structure of  $1\times 3\times 1$   $\text{NH}_4\text{V}_4\text{O}_{10}$  supercell with labelling of different oxygens. O1 is a two-coordinate oxygen and O3 only bond with one vanadium. O4 is three-coordinate oxygen. O2, O5, O6, and O7 have additional hydrogen bonds with  $\text{NH}_4^+$ .

As the interaction (hydrogen bonds) between  $\text{NH}_4^+$  and oxygen is weak compared to chemical bonds, we choose different oxygens with different coordination numbers and those form hydrogen bonds with  $\text{NH}_4^+$  for defect calculations. Those oxygens are labeled in Figure 4. The

formation energy of oxygen point vacancies was calculated and listed in Table 1 according to the equation:

$$E_f = E_{(NVO (VO))} + 1/2E_{(O_2)} - E_{(NVO)} \quad (1)$$

where  $E_f$  is the formation energy of oxygen vacancy defects in the NVO supercell.  $E_{(O_2)}$  is the energy of oxygen molecules,  $E_{(NVO (VO))}$  and  $E_{(NVO)}$  are the energies of NVO with or without oxygen vacancies.

**Table 1.** The formation energies of different oxygen point vacancies calculated by GGA+U functional.

Label	Formation energy (eV)
O1	1.89
O2	2.37
O3	2.49
O4	2.03
O5	2.53
O6	1.81
O7	1.83

The formation energies range from 1.81~2.53 eV, which indicates that the formation process of oxygen point vacancies was endothermic. The lowest formation energy corresponding to the removal of O6 is 1.81 eV. For O7, O1, and O4 sites, the values are 1.83, 1.89, and 2.03 eV, respectively. These values are close to that of the O6 site. The O6 has one-coordinated vanadium and one hydrogen bond. The coordination environment of O7 is similar to O6 but it is close to another  $NH_4^+$ . The O1 is coordinated with two vanadium ions. As the similarity of coordination number and local environments is low for each structure, we calculated the projected density of states (PDOS) and the total density of states (TDOS) of perfect NVO and NVO with different oxygen point vacancies to identify the fundamentals of the low defect formation energy.

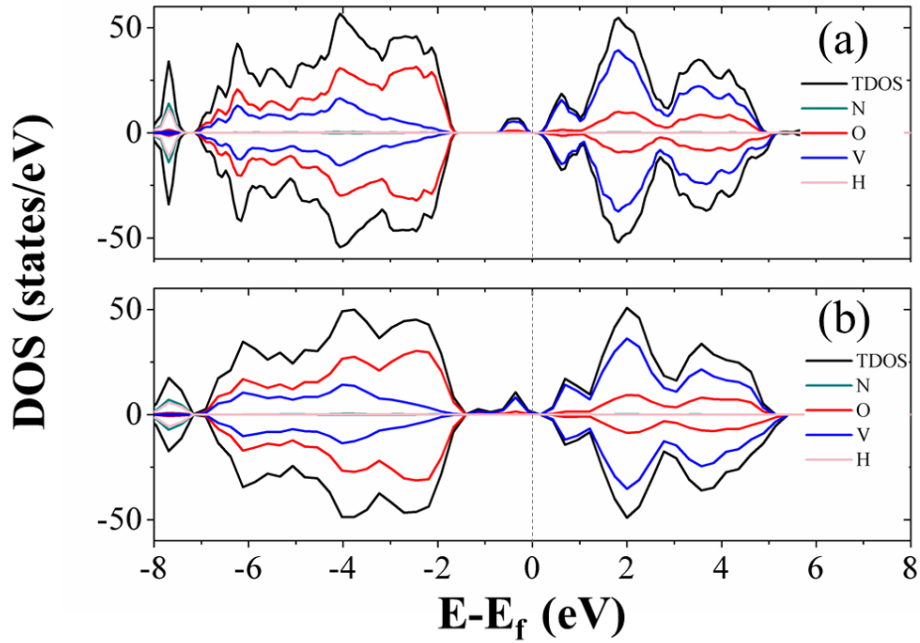


**Figure 5.** The projected density of states (PDOS) and the total density of states (TDOS) of (a) perfect NVO and NVO with oxygen point vacancy of (b) O6. The dotted lines denote the Fermi levels.

As electrons are liberated when an oxygen vacancy is formed, NVO presents *n*-type characteristics with oxygen point vacancy. As shown in Figure 5b, the defect states (gap states) of NVO with O6 site vacancies is closer to the Fermi level than perfect NVO (Figure 5a). The defect states close to the conduction band minimum (CBM) than perfect in NVO and hence make it a better donor. Thus, it is easier for electrons to be excited into the conduction band from the donor level, which increases the electronic conductivity of NVO with oxygen vacancies. In Fig. S13, it is found that the rest of the TDOS of O1, O4, and O7 sites also have two peaks (defect states) at around -1~0 eV below the Fermi level. The average defect formation energy for those with more peaks below the Fermi level is 1.89 eV, while the average defect formation energy for the rest of oxygen point vacancies (only show one peak at around 0.5 eV) is 2.46 eV. The gap in value is 0.57 eV. When O1, O4, O6, and O7 are extracted, the TDOS indicates that more vanadium ions are reduced. We also calculated the corresponding spin densities for perfect NVO and reduced NVO with an oxygen vacancy at the O1, O2, O3,

O4, O5, O6, and O7 sites to verify our explanation as shown in Figure 6. When the spin density of perfect NVO is used as a reference, it is clear that the oxygen point vacancies of O1, O4, O6, and O7 sites could produce more localized electron than the O2, O3 and O5 sites. Those oxygen point vacancies yield localized electrons on the additional two vanadium sites neighboring the vacancy than perfect NVO, while there is only one vanadium with localized electrons for O2, O3, and O5 sites compared with perfect NVO. In summary, when oxygen point vacancies are formed, those localized electrons stabilize the system and make the total energy decrease. The O6 vacancy is the most stable oxygen point vacancy because it produces more localized electrons around it and hence the most likely to take part in the reduction of NVO. The formation of oxygen point vacancy in NVO decreases the potential electrostatic attraction with  $Zn^{2+}$ . On the other hand, due to the strong electrostatic interaction of  $Zn^{2+}$ , the accumulation of localized electrons also forcefully facilitates the reversible  $Zn^{2+}$  de-intercalation with thermoneutral Gibbs free energy.<sup>33</sup> Eventually, these two factors effectively increase the reversibility of the  $Zn^{2+}$  insertion/extraction processes and thus enhance capacity and rate performance. Therefore, the corresponding DFT results convincingly confirmed the observations from electrochemical properties shown from the experimental results.

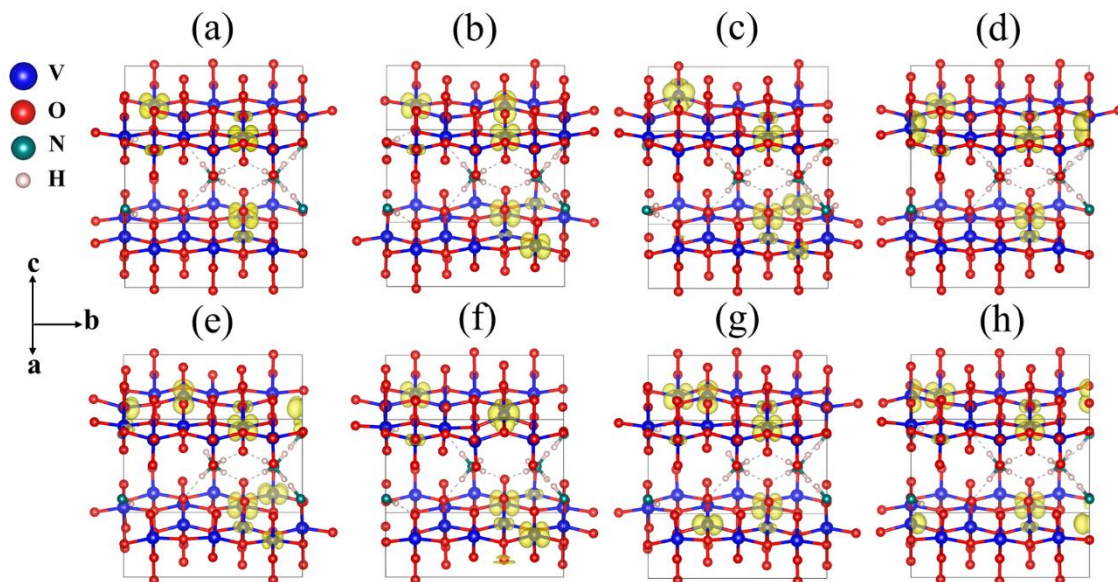


**Figure 6.** Spin densities for (a) perfect NVO and reduced NVO with an oxygen vacancy at (b)

O1, (c) O2, (d) O3, (e) O4, (f) O5, (g) O6 and (h) O7 sites. The isosurface shown is set at 0.01 electrons Å<sup>-3</sup>.

Additionally, to investigate the effect of oxygen vacancy in NVO for ion transport performance, the minimum energy migration pathways and barriers for Zn ions with both perfect and defective-NVO were investigated by using the CI-NEB method.<sup>64</sup> Previous study of NVO found that the diffusion process along the 001 orientation has extremely high energy barrier of 2.89 eV.<sup>65</sup> So, here the most stable and the metastable insertion sites of Zn ion were chosen for diffusion path along the 010 orientation and the specific structures are shown in Fig. S14. The insertion energy of Zn ion in perfect and defective-NVO were calculated and used to determine the most and metastable insertion site as follows:

$$E_{in} = E_{NVO-Zn} - E_{NVO} - E_{Zn} \quad (2)$$

Where the  $E_{in}$  is the insertion energy of Zn ion,  $E_{NVO-Zn}$  is the total energy of perfect and defective-NVO with the insertion of Zn ion.  $E_{NVO}$  is the total energy of perfect and defective-NVO.  $E_{Zn}$  is the energy of bulk Zn.

**Table 2.** The insertion energy ( $E_{in}$ ) of Zn ion of the most stable, metastable, and those near defect sites in perfect and defective-NVO.

Label	$E_{in}$ (eV)	Label	$E_{in}$ (eV)
Perfect-NVO		Defective-NVO	
4	1.17	Defect-site	1.10
5	0.71	5	0.70
6	0.98	6	0.85

In Table 2, the defect site in defective-NVO means the insertion site close to the oxygen vacancy, and the insertion site of 4 in perfect-NVO is similar to the defect site. When comparing the insertion energy of Zn ion of those insertion sites in perfect and defective-NVO, we found that oxygen vacancy is favorable for the insertion of Zn ion with lower insertion energy during intercalation process and the highest value of reduction reach up to 0.13 eV. This agrees with the opinion of a previous study that it is beneficial to the diffusion process for more smooth potential energy surface.<sup>33</sup> Subsequently, the corresponding minimum energy migration paths

prove this in Figure 7. The diffusion barrier in perfect-NVO is 0.82 eV, while the diffusion barrier in defective-NVO is 0.58 eV. The introduction of oxygen vacancy significantly decreases the diffusion barrier of Zn ion in defective-NVO.

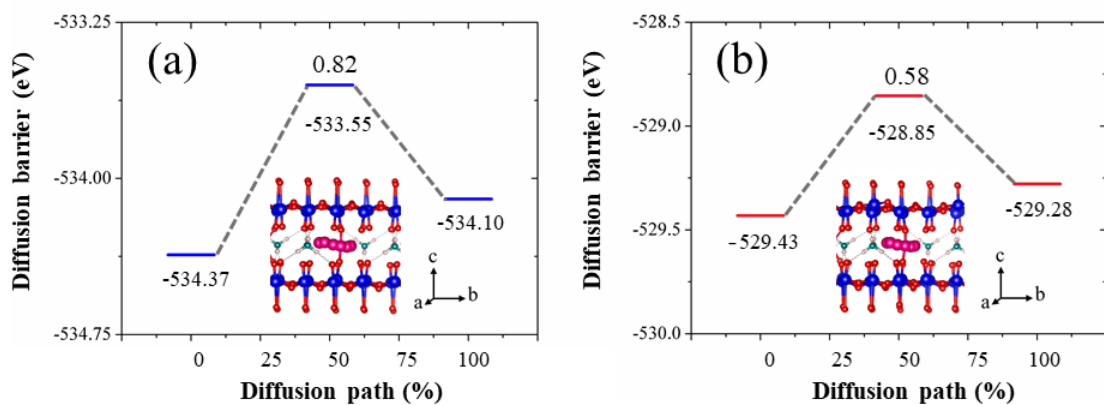


**Figure 7.** The diffusion barrier and minimum energy migration path of Zn ion in (a) perfect-NVO and (b) defective-NVO. The blue, red, green, fuchsia and light pink spheres represent V, O, N, Zn, and H, respectively.

## Conclusion

Through defects engineering from inducing cation, interlayer water and anionic vacancies within vanadium bronze materials, we successfully delivered a proof-of-concept demonstration on designing high-performance cathode materials for AZIBs. The tailored  $O_d\text{-NVO}\cdot n\text{H}_2\text{O}$  cathode achieved a high specific capacity of  $435\text{ mAh g}^{-1}$  at  $0.2\text{ A g}^{-1}$ , and  $244\text{ mAh g}^{-1}$  at  $10\text{ A g}^{-1}$  after 1500 cycles with negligible capacity decay. In particular, an extraordinary rate capability of 43% capacity retention after a 28 folds increase of current densities from  $0.5\text{ A g}^{-1}$  to  $14\text{ A g}^{-1}$  was attained. Additionally, the corresponding electrochemical properties were comprehensively evaluated by *ex-situ* characterizations and DFT simulations, which revealed encouraging  $\text{Zn}^{2+}$  kinetics and superior reversibility embodied with a transformation of capacitive-dominated energy storage behavior compared with pristine NVO cathodes. Indeed, the DFT results adequately elaborated different possibilities for oxygen-deficient sites and their contributions to facilitate  $\text{Zn}^{2+}$  diffusion properties. Meanwhile, the calculated density of states also suggested improved conductivity for  $O_d\text{-NVO}\cdot n\text{H}_2\text{O}$ . Hence, inducing multitype defects offers a feasible avenue to regulate the electronic structures and microstructures of vanadium-

based cathodes towards advanced energy storage applications

### **Acknowledgement**

This work is supported by the National Natural Science Foundation of China (Grant No. 21703248; 51602193), the Strategic Priority Research Program of the Chinese Academy of Sciences (Grant No. XDB20000000), Engineering and Physical Sciences Research Council (EPSRC, EP/L015862/1, EP/R023581/1), STFC Batteries Network (ST/R006873/1) and Shanghai “Chen Guang” project (16CG63).

### **Author Contribution**

J. L. and N. L. contributed equally. G.C., G.H., I.P.P. and J. L. designed the project; J.L. and F.W. performed the materials synthesis; J.L. tested the battery performance; N.L. carried out DFT calculations; S.Z. and J.G. performed materials characterization; J.L, Z.L. and W.L., P.R.S., D.J.L.B. and C.J.C conducted the data analysis; G.C., G.H. and I. P. P. directed the project; J.L., G.C., G.H. co-wrote the paper and all authors contributed to the revision of the draft.

### **Reference**

- 1 N. Günter and A. Marinopoulos, *Journal of Energy Storage*, 2016, **8**, 226–234.
- 2 F. Zheng, M. Kotobuki, S. Song, M. O. Lai and L. Lu, *J. Power Sources*, 2018, **389**, 198–213.
- 3 Y. Gong, K. Fu, S. Xu, J. Dai, T. R. Hamann, L. Zhang, G. T. Hitz, Z. Fu, Z. Ma, D. W. Mcowen, X. Han, L. Hu and E. D. Wachsman, *Mater. Today*, 2018, **21**, 594–601.
- 4 B. Safe, L. Suo, O. Borodin, Y. Wang, X. Rong, W. Sun, X. Fan, S. Xu, M. A. Schroeder, A. V Cresce, F. Wang, C. Yang, Y. Hu, K. Xu and C. Wang, *Adv. Energy Mater.*, 2017, **7**, 1701189.
- 5 M. R. Lukatskaya, J. I. Feldblyum and D. G. Mackanic, *Energy Environ. Sci.*, 2018, **11**, 2876–2883.
- 6 J. Gon, B. Son, S. Mukherjee, N. Schuppert, A. Bates, O. Kwon, M. Jong, H. Yeol and

- S. Park, *J. Power Sources*, 2015, **282**, 299–322.
- 7 C. Sun, J. Liu, Y. Gong, D. P. Wilkinson and J. Zhang, *Nano Energy*, 2017, **33**, 363–386.
- 8 L. Suo, O. Borodin, W. Sun, X. Fan, C. Yang, F. Wang, T. Gao, Z. Ma, M. Schroeder, A. Von Cresce, S. M. Russell, M. Armand, A. Angell, K. Xu and C. Wang, *Angew. Chem., Int. Ed.*, 2016, **85287**, 7136–7141.
- 9 H. Chen, Z. Zhang, Z. Wei, G. Chen, X. Yang, C. Wang and F. Du, *Sustainable Energy Fuels*, 2020, **4**, 128–131.
- 10 F. Wang, O. Borodin, T. Gao, X. Fan, W. Sun, F. Han, A. Faraone, J. A. Dura, K. Xu and C. Wang, *Nat. Mater.*, 2018, **17**, 543–549.
- 11 M. Song, H. Tan, D. Chao and H. J. Fan, *Adv. Funct. Mater.*, 2018, **28**, 1–27.
- 12 J. Ming, J. Guo, C. Xia, W. Wang and H. N. Alshareef, *Mater. Sci. Eng. R Reports*, 2019, **135**, 58–84.
- 13 C. Li, X. Zhang, W. He, G. Xu and R. Sun, *J. Power Sources*, 2020, **449**, 227596.
- 14 W. Xu and Y. Wang, *Nano-Micro Lett.*, 2019, **11**, 90.
- 15 B. Tang, L. Shan, S. Liang and J. Zhou, *Energy Environ. Sci.*, 2019, **12**, 3288–3304.
- 16 D. Xiong, X. Li, Z. Bai and S. Lu, *Small*, 2018, **14**, 1703419.
- 17 L. Peng, Y. Zhu, D. Chen, R. S. Ruoff and G. Yu, *Adv. Energy Mater.* 2016, **6**, 1600025
- 18 J. Zhao, H. Ren, Q. Liang, D. Yuan, S. Xi, C. Wu, W. Manalastas, J. Ma, W. Fang, Y. Zheng, C. Du, M. Srinivasan and Q. Yan, *Nano Energy*, 2019, **62**, 94–102.
- 19 K. D. Rasamani, F. Alimohammadi and Y. Sun, *Materials Today*, 2017, **20**, 83-91.
- 20 X. Sun, V. Du, B. L. Mehdi, N. D. Browning and L. F. Nazar, *Chem. Mater.*, 2016, **28**, 534-542.
- 21 J. L. Andrews, S. Singh, C. Kilcoyne, P. J. Shamberger, G. Sambandamurthy and S. Banerjee, *MRS Commun.*, 2017, **7**, 634–641.
- 22 D. Selvakumaran, A. Pan, S. Liang and G. Cao, *J. Mater. Chem. A*, 2019, **7**, 18209–18236.
- 23 X. Yao, Y. Zhao, F. A. Castro and L. Mai, *ACS Energy Lett.*, 2019, **4**, 771–778.
- 24 J. Li, K. McColl, X. Lu, S. Sathasivam, H. Dong, L. Kang, Z. Li, S. Zhao, A. G.

- Kafizas, R. Wang, D. J. L. Brett, P. R. Shearing, F. Corà, G. He, C. J. Carmalt and I. P. Parkin, *Adv. Energy Mater.*, 2020, **10**, 2000058.
- 25 J. Zhou, L. Shan, Z. Wu, X. Guo, G. Fang and S. Liang, *Chem. Commun.*, 2018, **54**, 4457–4460.
- 26 H. Maleki, K. Sari and X. Li, *Adv. Energy Mater.*, 2019, **9**, 1901597
- 27 D. Li, S. Lu, A. Koo, K. Adair and X. Sun, *Nano Energy*, 2018, **44**, 111-120.
- 28 F. Wang, W. Sun, Z. Shadike, E. Hu, X. Ji, T. Gao, X. Yang, K. Xu and C. Wang, *Angew. Chem., Int. Ed.*, 2018, **57**, 11978-11981.
- 29 D. Kundu, S. H. Vajargah, L. Wan, B. Adams, D. Prendergast and L. F. Nazar, *Energy Environ. Sci.*, 2018, **11**, 881-892.
- 30 J. Lai, H. Zhu, X. Zhu, H. Koritala and Y. Wang, *ACS Appl. Energy Mater.*, 2019, **2**, 1988–1996.
- 31 M. Yan, P. He, Y. Chen, S. Wang, Q. Wei, K. Zhao, X. Xu, Q. An, Y. Shuang, Y. Shao, K. T. Mueller, L. Mai, J. Liu and J. Yang, *Adv. Mater.*, 2018, **30**, 1703725.
- 32 F. Wan and Z. Niu, *Angew. Chem., Int. Ed.*, 2019, **58**, 16358-16367.
- 33 Z. Batteries, M. Liao, J. Wang, L. Ye, H. Sun, Y. Wen, C. Wang, X. Sun, B. Wang and H. Peng, *Angew. Chem.*, 2020, **132**, 2293-2298.
- 34 Z. Li, Y. Ren, L. Mo, C. Liu, K. Hsu, Y. Ding, X. Zhang, X. Li, L. Hu, D. Ji and G. Cao, *ACS Nano*, 2020, **14**, 5581–5589.
- 35 L. Cheng, M. Xu, Q. Zhang, G. Li, J. Chen and Y. Lou, *J. Alloys Compd.*, 2019, **781**, 245–254.
- 36 Y. Zhang, J. Zheng, Y. Zhao, T. Hu, Z. Gao and C. Meng, *Appl. Surf. Sci.*, 2016, **377**, 385–393.
- 37 E. A. Esparcia, M. S. Chae, J. D. Ocon and S. Hong, *Chem. Mater.*, 2018, **30**, 3690–3696.
- 38 Y. Liu, B. Shen, X. Liu, Y. Wu, X. He and Q. Li, *Int. J. Electrochem. Sci.*, 2017, **12**, 5483–5491.
- 39 Y. Xu, H. Dong, M. Zhou, C. Zhang, Y. Wu, W. Li, Y. Dong and Y. Lei, *Small Methods*, 2018, **1800349**, 1800349.
- 40 A. M. El-sayed, S. Mohamed and A. Mousa, *J. Chin. Chem. Soc.*, 2006, **5**, 559–565.

- 41 A. Qian, K. Zhuo, M. S. Shin, W. W. Chun, B. N. Choi and C. Chung, *ChemSusChem*, 2015, **8**, 2399 – 2406
- 42 Y. Yang, Y. Tang, S. Liang, Z. Wu, G. Fang, X. Cao, C. Wang, T. Lin, A. Pan and J. Zhou, *Nano Energy*, 2019, **61**, 617–625.
- 43 D. Kundu, B. D. Adams, V. Duffort, S. H. Vajargah and L. F. Nazar, *Nat. Energy*, 2016, **1**, 1–8.
- 44 V. Bondarenka, H. Tvardauskas, M. Senulis, A. Pašiškevičius and S. Grebinskij, *Acta Phys. Pol., A*, 2011, **119**, 135–136.
- 45 W. Li, D. Kong, T. Yan, M. Shi, D. Kong and Y. Feng, *J. Solid State Chem.*, 2020, **286**, 121296.
- 46 C. Lv, C. Yan, G. Chen, Y. Ding, J. Sun and Y. Zhou, *Angew. Chem., Int. Ed.*, 2018, **57**, 6073–6076.
- 47 M. Huang, J. Bian, W. Xiong and R. Zhang, *J. Mater. Chem. A*, 2018, **6**, 3602–3609
- 48 B. Guo, L. Chen, S. Shi, A. Ishaq, D. Wan, Z. Chen, L. Zhang, H. Luo and Y. Gao, *RSC Adv.*, 2017, **7**, 10798–10805.
- 49 M. Yan, P. He, Y. Chen, S. Wang, Q. Wei, K. Zhao, X. Xu, Q. An, Y. Shuang, Y. Shao, K. T. Mueller, L. Mai, J. Liu and J. Yang, *Adv. Mater.*, 2018, **30**, 1–6.
- 50 Y. Yang, Y. Tang, G. Fang, L. Shan, J. Guo, W. Zhang, C. Wang, L. Wang, J. Zhou and S. Liang, *Energy Environ. Sci.*, 2018, **11**, 3157–3162.
- 51 B. Tang, J. Zhou, G. Fang, F. Liu, C. Zhu, C. Wang, A. Pan and S. Liang, *J. Mater. Chem. A*, 2019, **7**, 940–945.
- 52 P. He, G. Zhang, X. Liao, M. Yan, X. Xu, Q. An, J. Liu and L. Mai, *Adv. Energy Mater.*, 2018, **8**, 1–6.
- 53 L. Shan, Y. Yang, W. Zhang, H. Chen, G. Fang, J. Zhou and S. Liang, *Energy Storage Mater.*, 2019, **18**, 10–14.
- 54 S. Islam, M. H. Alfaruqi, B. Sambandam, D. Y. Putro, S. Kim, J. Jo, S. Kim, V. Mathew and J. Kim, *Chem. Commun.*, 2019, **55**, 3793–3796.
- 55 T. Wu, K. Zhu, C. Qin and K. Huang, *J. Mater. Chem. A*, 2019, **7**, 5612–5620.
- 56 C. Xia, J. Guo, P. Li, X. Zhang and H. N. Alshareef, *Angew. Chemie. Int. Ed.*, 2018, **57**, 3943–3948.

- 57 B. Sambandam, V. Soundharrajan, S. Kim, M. H. Alfaruqi, J. Jo, S. Kim, V. Mathew, Y. K. Sun and J. Kim, *J. Mater. Chem. A*, 2018, **6**, 3850–3856.
- 58 C. Xia, J. Guo, Y. Lei, H. Liang, C. Zhao and H. N. Alshareef, *Adv. Mater.*, 2018, **30**, 1–7.
- 59 W. Li, K. Wang, S. Cheng and K. Jiang, *Energy Storage Mater.*, 2018, **15**, 14–21.
- 60 B. Tang, G. Fang, J. Zhou, L. Wang, Y. Lei, C. Wang, T. Lin, Y. Tang and S. Liang, *Nano Energy*, 2018, **51**, 579–587.
- 61 G. He, M. Qiao, W. Li, Y. Lu, T. Zhao, R. Zou, B. Li, J. A. Darr, J. Hu, M.-M. Titirici and I. P. Parkin, *Adv. Sci.*, 2017, **4**, 1600214.
- 62 F. Ming, H. Liang, Y. Lei, S. Kandambeth, M. Eddaoudi and H. N. Alshareef, *ACS Energy Lett.*, 2018, **3**, 2602–2609.
- 63 B. Sambandam, V. Soundharrajan, S. Kim, M. H. Alfaruqi, J. Jo, S. Kim, V. Mathew, Y. Sun and J. Kim, *J. Mater. Chem. A*, 2018, **6**, 15530–15539.
- 64 G. Henkelman, B. P. Uberuaga and H. Jonsson, *J. Chem. Phys.* 2000, **113**, 9901.
- 65 Q. Li, X. Rui, D. Chen, Y. Feng, N. Xiao, L. Gan, Q. Zhang, Y. Yu and S. Huang, *Nano-Micro Lett.* 2020, **12**, 1-12.